

# Real-Time Surface Shape Sensing for Soft and Flexible Structures Using Fiber Bragg Gratings

Tian Le Tim Lun , Kui Wang , Justin D. L. Ho , Kit-Hang Lee , Kam Yim Sze ,  
and Ka-Wai Kwok , *Senior Member, IEEE*

**Abstract**—In this letter, we present a new soft and flexible sensor which can reconstruct its surface shape in real time. A single-core optical fiber with fiber Bragg gratings (FBGs) is capable of detecting sparse local strains at high bandwidth using wavelength-division multiplexing. The fiber was embedded into an elastomeric substrate to reconstruct its global surface morphology. Finite element analysis was used to determine the design parameters, and also to validate the unique mapping from sparse strain measurements to the continuum shape of the sensor. To simplify the fabrication and error compensation process without precise/prior knowledge of the FBG locations in the sensor, machine learning-based modeling was applied. This enables real time, robust and reliable shape reconstruction. It is demonstrated to outperform various applications of electronics-based sensors, which require sophisticated electrode wiring and noise reduction. Experiments were performed to evaluate the sensing accuracy and repeatability.

**Index Terms**—Fiber bragg gratings, flexible robots, soft sensors and actuators, surface shape sensing.

## I. INTRODUCTION

IN RECENT years, there has been a trend towards integrating soft and deformable structures into robotic systems. Target applications include surgery [1] and rehabilitation [2], where researchers take advantage of soft and flexible robots for their inherent mechanical compliance. However, these soft robotic systems are often controlled with feedback from either large tracking systems, using indirect variables (e.g., pressure in fiber-reinforced actuators), or in an open loop, neglecting the fact that actual robot shape and posture are inevitably affected by the environment [3].

As a result, measurement of the surface shape itself has become an area of interest. Some research utilize non-contact external equipment such as stereo cameras and LiDAR to reconstruct 3D surfaces [4]. Motion capture systems have also

been employed to collect the local position information of subjects, with reflective markers attached to the surface [5], [6]. Gelsight [7] was able to use external CCD cameras with visual processing techniques to reconstruct complex surfaces from image frames. Similarly, GelForce [8] uses CCD cameras to detect the displacement of markers in a flexible substrate to estimate surface traction fields. Although high-resolution sensing data from camera-based systems allows reconstruction of complex deformations, these kinds of systems are inconvenient to be used in soft robotics or stand-alone robotic systems due to their bulkiness and dependence on line-of-sight.

The use of self-contained shape sensors is another approach to measuring flexible 3D objects. Small-sized contact-based sensors can be attached to objects for transducing the local position and orientation information. Microelectromechanical systems (MEMS) allow the integration of many miniaturized sensors to provide local information for global shape reconstruction [9]. Surface shape reconstruction has been performed with a non-stretchable sheet of three-axis accelerometers arranged in a grid pattern [10]. Similarly, Cheng *et al.* [11] developed an artificial skin that consisted of rigid hexagonal sensor units based on accelerometers, which could provide the relative pose of each sensor. Saguin-prynski *et al.* [12] described their work on 3D curve reconstruction from orientation measurements, and applied multiple curves for surface reconstruction. However, a limitation of grid-type MEMS sensors is that they often have limited flexibility and stretchability due to fixed connections between nodes. Due to wiring, they are also complicated for large-scale applications.

More recently, liquid conductors, e.g., eutectic Gallium Indium (eGaIn) have been embedded in elastomeric substrates to measure strain in fully-soft sensors. These sensors are inherently compliant and have been designed as artificial skins that can be integrated into completely soft systems, like soft robots [13, 14]. Their underlying sensing principle is similar to traditional strain gauges, requiring contact electrodes on either end of the liquid-metal channels. This can make scaling to larger or more complex designs a challenging task.

Optical fiber-based sensors using fiber Bragg gratings (FBGs) are one of the sensor technologies that have proven performance in fields like civil engineering [15] and aerospace industries [16]. FBGs have excellent electromagnetic immunity [17] and can be used in harsh environment [18], such as extreme high electromagnetic noise, vacuum and extremely low temperature. They can carry a high density of sensors on a single fiber [19]

Manuscript received September 10, 2018; accepted December 26, 2018. Date of publication January 14, 2019; date of current version February 19, 2019. This letter was recommended for publication by Associate Editor V. Ho and Editor A. M. Okamura upon evaluation of the reviewers' comments. This letter was supported in part by the Croucher Foundation and in part by the Research Grants Council (RGC) of Hong Kong (Ref. no.: 17202317, 17227616, and 27209515). (Tian Le Tim Lun, Kui Wang, and Justin D.L. Ho are co-first authors.) (Corresponding author: Ka-Wai Kwok.)

The authors are with the Department of Mechanical Engineering, The University of Hong Kong, Hong Kong (e-mail: timlun@connect.hku.hk; kuiwang@connect.hku.hk; jdlho@connect.hku.hk; brian.khl@hku.hk; kysze@hku.hk; kwokkw@hku.hk).

This letter has supplementary downloadable material available at <http://ieeexplore.ieee.org>, provided by the authors.

Digital Object Identifier 10.1109/LRA.2019.2893036

with small form factor and long-term stability [20]. 3D curve-based shape reconstruction based on FBG sensing has been increasingly applied for continuum robots [21], such as steerable interventional needles for biopsy and ablation [22]. However, these methods were specified for tube-shaped reconstruction, where FBGs are used to monitor the 3D curvature. To extend the application of FBGs in shape sensing, more designs have been proposed. Silva *et al.* [23] designed a wearable sensing glove for monitoring hand gestures and postures, in which a single FBG fiber was laid across a hand in a curvilinear layout. In this design, the glove was able to show the hand motion in real time, however, this was achieved by measuring the bending angle of each finger joint, not from the shape of the hand itself. This creates dependence on the accurate placement of FBGs so that they align with the patient's finger joints. Mable *et al.* [24] implemented a dual-layer FBG mesh in their 3D shape sensor. It requires precise fixture of FBG allocation, where the two fiber layers must be aligned such that each FBG is overlaid exactly on each other at 90°. Zhang *et al.* [25] provided surface shape reconstruction algorithm for a large scale (800 × 800 mm) plate surface, with a net of orthogonal FBG strain sensors. The sensor can detect both convex and concave object surfaces, however, the use of a relatively rigid Plexiglas substrate limits the deformation to simple shapes. Additionally, for shape sensors employing orthogonal fiber layouts, the stretchability of the overall sensor substrate is limited, and depends on precise FBG positioning that strongly affects the reconstruction accuracy [26].

In this letter, we design and fabricate a new flexible 3D shape sensor which can reconstruct the surface of the subject in real-time. Unlike most optical fiber-based shape sensors that can only measure the curvature change along the fiber, the proposed sensor can measure the complete 3D shape of its surface deformed by bending and twisting. A single fiber with sparsely distributed FBGs is embedded into a flat silicone rubber plate and used to measure strains on both top and bottom surfaces. Through finite element analysis (FEA), we consider the effect of design parameters and validate the uniqueness of strain-to-shape mapping. The overall deformation is mapped to the optical signals using a machine learning approach. Although this introduces a dependence on the obtained training data, this approach can compensate for fabrication errors while eliminating the need for complex modeling and stringent allocation of FBGs. The presented sensor layout and design are easily tailor-made to specific applications. The main contributions of this letter are:

- 1) Development of a design framework for FBG-based surface morphology sensors. A single-core optical fiber with sparsely distributed FBGs was used to detect surface morphology in real-time.
- 2) FEA to determine sensor design parameters with embedded FBGs. The mapping between surface deformation and fiber responses were proven to be unique for the proposed fiber layout.
- 3) Machine learning-based modelling to enable more robust and reliable shape reconstruction without explicit knowledge of the FBG configuration/allocation.

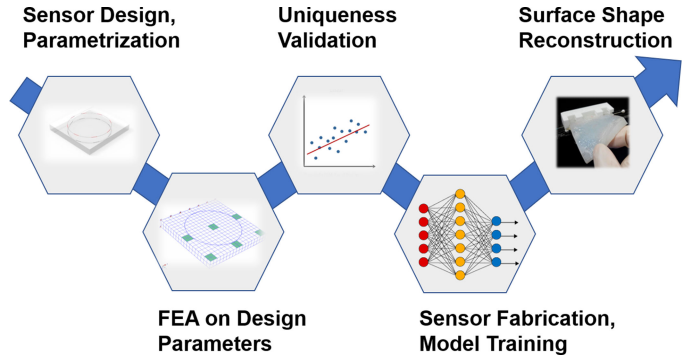


Fig. 1. Workflow of the proposed surface shape sensing approach.

## II. SENSOR DESIGN AND STRAIN DATA ANALYSIS

To prototype our surface shape sensor, we propose key design considerations, followed by parametric studies using FEA. The shape reconstruction, namely the mapping from local strain to shape, is simulated. Such a mapping is proven unique through our data-driven approach. Finally, the sensor is fabricated and tested with the physical parameters suggested. The overall workflow of our study is illustrated in Fig. 1.

### A. Surface Shape Sensor Design

#### 1) Design Considerations

**Flexibility** – Sensors that integrate with soft, flexible structures must be adequately flexible to not inhibit the motion of the original structure. In particular for soft robotics, this integration should not alter the deformation actuated by the soft actuators. A thin optical fiber of  $\phi 195 \mu\text{m}$  ensures promising compliance with such morphological deformation, compared to electronics-based sensors that require complicated electrode wiring and that are inherently rigid. A single-core fiber has a high capability of multiplexing strain measurements through multiple FBGs. In our sensor design, each FBG should be short to detect local strain. The distribution of such strain sensing would be critical to reconstruct the shape in detail.

**Stretchability** – Stretching is a common form of deformation, especially for the motion of soft robots. Surface shape sensors are typically designed with grid-form sensing networks, however, this configuration can limit the degree of flexibility and stretchability especially when unavoidable in-plane loading exists, particularly in soft robots. Our proposed fiber layout in the sensor allows stretchability along different directions, and silicone rubber is chosen as the substrate layer for high compliance and firm bonding with common soft robots fabricated with silicone.

**Reliability** – The reliability of the sensor over time would define its usage in practical applications. FBGs provide excellent durability in harsh environments including dramatic temperature changes and chemical corrosions [27]. However, FBG-written fiber is still fragile under concentrated loading. In this letter, Draw Tower Gratings (DTGs) are selected instead of conventional strip-and-recoat FBGs, as they offer over four times the mechanical strength.

## 2) FBG Sensing Principle

The proposed sensing principle of our flexible shape sensor is based on the mapping between the local strains and global displacements. When the sensor is deformed by bending, twisting or other forms of deformation, the embedded FBG sensors are strained accordingly. The decomposed axial strains along the fiber are then converted to optical signals in which different strains would result in different wavelength components measured by the optical interrogator.

The shift in central wavelength of the each FBG depends on the effective refractive index and the grating period which are a function of temperature and strain. Therefore, the sensing response varies when our proposed sensor experiences temperature changes or under external forces. The mechanical strains change the grating period and the effective refractive index, resulting in shifts in Bragg wavelengths [28]. Including the effect of temperature, this allows strain and temperature measurements by the reflected FBG spectrum in real-time. This dependency is described as follows:

$$\frac{\Delta\lambda}{\lambda_0} = k\varepsilon + \alpha_\delta\Delta T \quad (1)$$

where  $\Delta\lambda$  is the wavelength shift,  $\lambda_0$  is the base wavelength at fabrication,  $k = 0.78$  is the gage factor,  $\alpha_\delta$  is the change of refraction index and  $\Delta T$  is the temperature change in K. The strain  $\varepsilon$  includes the mechanical-induced strain  $\varepsilon_m$  and the thermal strain  $\varepsilon_T$ . Substituting  $\varepsilon_T = \alpha_{sp}\Delta T$  into equation (1):

$$\frac{\Delta\lambda}{\lambda_0} = k\varepsilon_m + (k\alpha_{sp} + \alpha_\delta)\Delta T \quad (2)$$

where  $\alpha_{sp}$  is the coefficient of thermal expansion of the substrate material.

As the temperature has an impact on sensing signals, temperature compensation is performed to obtain precise mechanical strain measurements. An additional temperature grating is used to correct other strain measuring gratings. Substituting  $\varepsilon_m = 0$  into (2), its signal is calculated according to equation:

$$\frac{\Delta\lambda_c}{\lambda_{0c}} = (k\alpha_{sp} + \alpha_\delta)\Delta T \quad (3)$$

where  $\lambda_{0c}$  is the central wavelength of the compensation FBG.

For the FBGs used in mechanical strain sensing, (2) can be rewritten as:

$$k\varepsilon_m = \frac{\Delta\lambda_m}{\lambda_{0m}} - (k\alpha_{sp} + \alpha_\delta)\Delta T \quad (4)$$

and  $\lambda_{0m}$  is the central wavelength of the mechanical strain measuring FBG. Taking (3) into (4):

$$\varepsilon_m = \frac{1}{k} \left( \frac{\Delta\lambda_m}{\lambda_{0m}} - \frac{\Delta\lambda_c}{\lambda_{0c}} \right) \quad (5)$$

Shifted wavelengths due to the mechanical strain  $\varepsilon_m$  can be calculated by subtracting the signal of the temperature-compensation FBG from the signal of the active strain-measuring FBG.

## 3) Conceptual Design /Sensor Layout

As our first proof-of-concept sensor design, we chose a rectangular geometry for the sensor base to simplify its fabrication. The sensor base was molded from a silicone rubber square and

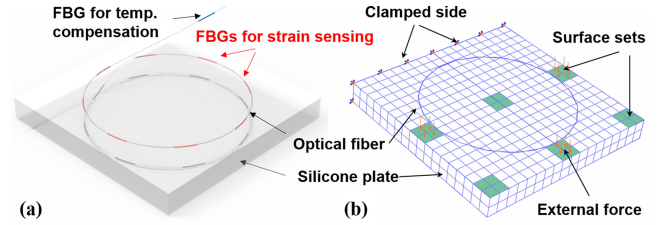


Fig. 2. (a) Overview of the proposed surface shape sensor structure: a single fiber is looped in two circles away from the midplane. Each circle contains 8 FBGs. (b) Finite element model of the sensor. The silicone plate is discretized into 3D 8-node continuum elements and the optical fiber is discretized into 3D 2-node truss elements. 12 surface sets (6 shown in green) are predefined to apply random pressure loadings for simulating the external forces.

the FBG sensor is circularly wrapped on the top and bottom of the sensor as shown in Fig. 2(a). The FBG fiber is placed away from the midplane to enable sensor response to bending deformation. The overall design includes five layers: the middle sensor base substrate layer, two FBG sensor layers and two silicone protection layers. The protection layers are thin coatings above the FBG layers and have a small effect on sensor flexibility. The FBG sensor layer is shaped in circular form to obtain the strain information.

## B. Parametric Study Using FEA

In our letter, we make use of FEA to analyze the relationship between the sensor global displacements and the local strains. Validation through FEA allows us to see the effect of parameters like sensor thickness, and to ensure unique sensor responses prior to fabrication. The side length of the square sensor was chosen to be 45 mm in our prototype. In this research, two selected parameters are studied with FEA. Proper fiber layer offset and sensor thickness are studied to evaluate the sensor performances. The estimated and predicted sensor responses of the sensor are computed with Abaqus 6.14.

### 1) FEA Modeling

The finite element model of the sensor is shown in Fig. 2(b). The silicone sensor base and the sensor fiber are modeled as 3D deformable models. The protection layers (0.2 mm thick) are not included in the simplified finite element model as it has a negligible effect on the uniqueness of the sensor response.

The silicone plate model is meshed to  $2 \times 18 \times 18$  C3D8RH elements and the sensor fiber is meshed to 44 T3D2H elements which are 2-node linear 3D trusses that only allow axial strains. For silicone rubber (Smooth On Ecoflex 0030), it is modeled as a hyperelastic material using Ogden strain energy potential. Parameters of the 3-term Ogden model are adopted from literature [29]:  $\mu_1 = 0.024361$ ,  $\mu_2 = 6.6703 \times 10^{-5}$ ,  $\mu_3 = 0.45381 \times 10^{-3}$ ,  $\alpha_1 = 1.7138$ ,  $\alpha_2 = 7.0679$ ,  $\alpha_3 = -3.3659$ ,  $D_1 = 3.2587$ ,  $D_2 = D_3 = 0$ , where  $\mu$ s,  $\alpha$ s and  $D$ s are temperature-dependent material parameters. The units for  $\mu$ s and  $D$ s are MPa and  $(\text{MPa})^{-1}$  respectively, whilst  $\alpha$ s are dimensionless. To model the mechanical behavior of the fiber, a linear elastic model is used with elastic modulus 70 GPa and Poisson's ratio 0.16 [30]. To simulate sensor response under different loading conditions, one edge of the sensor is prescribed



with the clamped condition while others are free. All the simulations are done under static loading steps. To generate deformations such as bending and twisting, surface loads are applied on twelve surface sets. They are arranged symmetrically on the top and bottom surface of the sensor, with those on the top surface (green) in Fig. 2(b).

## 2) Sensor Parameters Analysis

Other than the width of the sensor, two other key parameters of the sensor should be determined in advance, i.e., the fiber layer offset  $h$  and the sensor thickness  $t$ . According to the Kirchhoff plate theory, the material element would experience a strain which increases with the offset distance from the neutral plate. Simulation with FEA was also conducted and the results were in agreement. Therefore, to maximize the sensitivity of the sensor, the fiber layer offset was set to the maximum value, i.e., the two fiber layers would be put on the upper and lower surfaces of the substrate.

Since the fiber layers were selected to be on the surface of the sensor, the overall thickness governs both the sensor sensitivity and flexibility. To investigate the effect of changing sensor thickness, sensor responses were obtained through FEA such that the sensor was placed on two supporting pins and subjected to a loading force generated by a cylinder with radius 20 mm. At step = 1.0, the sensor is bent to the same radius by pushing the cylinder. For the soft and flexible sensor, the low thickness would be an advantage when integrating the sensor on actuators and other components for flexibility. However, as single core fiber is used in this letter, the fiber needs to be offset from the mid-plane and with a suitable thickness to differentiate between deformation patterns. The thickness  $t$  is determined by considering the strain patterns with varying thickness (2.5–7.5 mm). The range was selected by considering reasonable sensor thicknesses that would not inhibit flexible motions.

In Fig. 3, the strain responses of our proposed sensor structure are simulated under the same bending with several steps. When the sensor base thickness  $t$  is 2.5 mm, the compression strain responses are not significant enough to identify shape patterns due to the overlapping and may be altered by sensor noise. By increasing the sensor thickness, the output responses also increase and become noticeable. At  $t = 2.5$  mm, strains due to compressive loadings are overlapped at each simulation step. At  $t = 5$  mm, negative strains can be clearly identified and used to discriminate deformations. At  $t = 7.5$  mm, the sensitivity is further increased, with several acute points appearing. However, the flexibility would decrease when the thickness increases. After comparing the sensor responses with more deformation modes, 5 mm is selected as the sensor thickness of our primary shape sensor to yield distinct strain patterns while providing high flexibility. Depending on the application and sensing requirement, the sensor thickness can be adjusted for optimal performance.

## C. Data-Driven Uniqueness and Modeling

To reconstruct the surface from local strains, a model which could map from the strain data to the surface deformation is needed and the uniqueness of the mapping should be guaranteed. Conventional methods build kinematics models with complicated mathematical analysis, which typically require highly

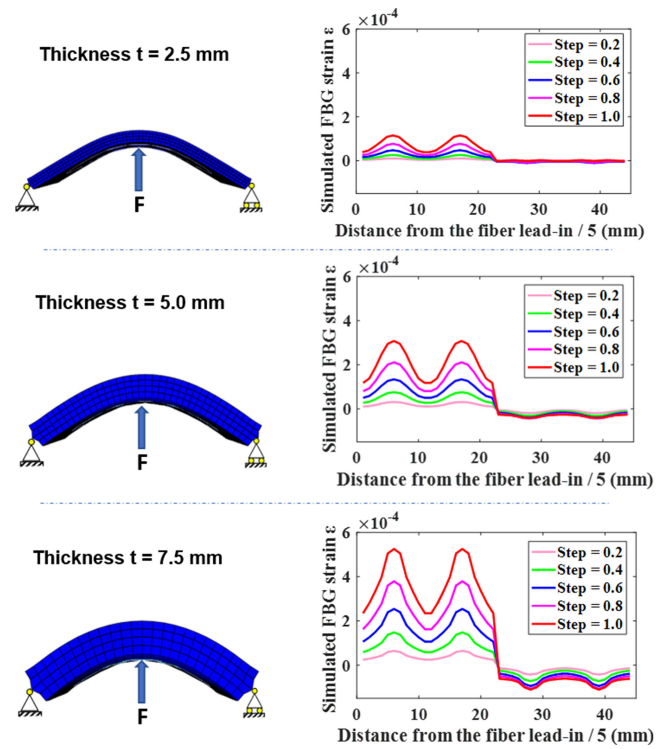


Fig. 3. Simulated strain response of three sensors with different thicknesses under 3-point bending. Fibers were placed at the top and bottom surfaces of the sensor. Strain responses were observed to increase with sensor thickness.

accurate fabrication or error compensation. We apply a data-driven approach, namely an artificial neural network (ANN), to tackle the modeling problem and for validation of the sensor's uniqueness.

From the modeling perspective, data-driven approaches are beneficial for compensating errors induced during fabrication, or when sensor positions are not explicitly known. It allows flexibility in fabrication and design, making it easier to customize the sensor to different applications. For validating the sensor's uniqueness, we use data generated from our FEA model to train a separate ANN. In both ANNs, a typical multilayer feedforward network with two layers is built, but different backpropagation methods are used for uniqueness validation and modeling. The hidden layer contains 10 neurons which connect to the inputs, and the second layer produces the network outputs.

### 1) Uniqueness Validation With FEA

Initially in our FEA validation, bending, twisting and random loading are tested to analyze the uniqueness of the model. Pressure loading was applied to the highlighted surfaces to cause deformation, as shown in Fig. 2(b). The use of pressure loading creates a smooth deformed surface without applying a concentrated force on a particular element or node. In Fig. 4, the deformation patterns and the corresponding strain response are shown and compared. Under different deformation patterns, the strain responses are notably different, indicating that different shapes could be reconstructed uniquely. Moreover, for the same shape in opposite directions (e.g., bending up vs bending down) similar strain response patterns are observed, but inversed, due to the double-layer fiber layout of the sensor. It is also noted for the same deformation pattern at different

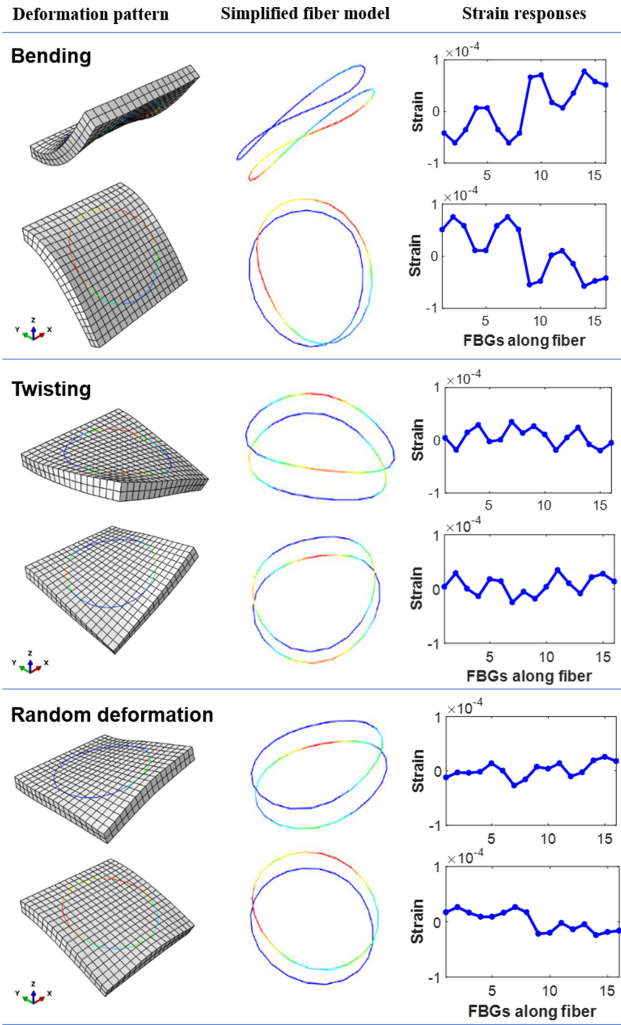


Fig. 4. Simulated fiber strains under three types of deformation. The 1st column depicts the deformed shape sensor. The 2nd column shows the strain induced in the fiber, where warmer the color indicates higher the strain induced. The 3rd column plots the overall strain patterns simulated for the FBGs.

magnitudes of deformation (e.g., the different steps simulated in Fig. 3), the overall strain response patterns remain the same, while the strain peaks increase with the deformation magnitude.

## 2) Uniqueness Validation With ANN

To further validate the sensor's uniqueness, a large number of simulated strain responses and corresponding surface displacement data were extracted from the FEA model for training of an ANN. Within a defined range of pressure, 729 simulations with random pressure loadings were gathered, where each contains 10 steps, thus 7290 data sets were generated. The inputs to the neural network are the 16 sparse axial strains in fiber truss elements and the output nodes are from 1083 ( $19 \times 19 \times 3$ ) displacement data. Scaled conjugate gradient backpropagation was used, since the network is large and requires less memory for calculations, whereas Levenberg-Marquardt (L-M) backpropagation was used for reconstructing the actual surface shape in Section III.

The neural network performance is evaluated by mean-squared-error (MSE) between the FEA-simulated displacement in the experiment and the output displacement from the trained

network. The training stops when the magnitude of performance gradient is less than  $1e^{-6}$  or the validation performance stop decreasing. Cross-validation is employed to prevent over-fitting in which 70% of the data is used for network training, 15% is used for validation and the last 15% is used for testing. The results showed a good fit with a  $R^2$  value of 0.989 and the overall errors are small. The high accuracy of regression implies that, within the sampled range, the relationship between the surface displacements and FBG strains is unique.

## D. Sensor Fabrication

### 1) Sensor Fabrication Procedure

The fabrication can be performed as the size and other parameters have been determined. Ecoflex silicones are chosen due to their low viscosity that favors mixing and de-airing in fabrication. A mixed portion of silicones are degassed and injected into 3D-printed molds which are coated with releasing agent. After demolding the patterned silicone plate, the top and bottom surfaces of the plate are penetrated with a needle for passing the fiber. Since stresses are induced by shaping the fiber to target configuration, small pins are used to temporarily fix the fiber shape on the silicone plate, preventing the fiber from returning to its neutral position. A thin layer of ELASTOSIL® E41 is applied to partially seal the optical fiber and silicone plate. Finally, the pins are removed and two thin silicone coatings (same material as silicone plate) are placed and bonded firmly on the top and bottom surface of the silicone plate as protective layers.

In the proposed sensor layout, the embedded fiber is wound in a circular fashion, which means that the center and corners of the sensor have no underlying FBGs. For any local deformation that occurs on the side of the sensor, strains will still be imparted to the nearby FBGs due to the inherent stiffness of the silicone substrate. For deformations at the center of the sensor, it is expected to generate global grating responses but with lower magnitude, since the gratings are surrounding the center but not aligned with the resultant strain in the FBGs.

### 2) Detailed Fiber Specifications

The FBGs embedded in the silicone plate are made from intense ultraviolet light exposure on the optical fiber core. A fixed index modulation, i.e., a grating, is created and increased the core refractive index permanently. The fiber has a cladding diameter of  $125 \mu\text{m}$  and is coated with Ormocer (a diameter of  $195 \mu\text{m}$ ). Each grating has a length of 5 mm where smaller lengths are also available in practice. Each grating is separated with a 10 mm gap for the first 16 FBGs and 450 mm between 16th and 17th FBG. 16 FBGs covered two surfaces of the silicone plate to capture strain information and the remaining FBG is used as a temperature compensation sensor. FBGs with shorter wavelengths are located nearer to the lead-in end. The number of gratings, the separation between gratings, and fiber length can be tailor-made for each desired application, providing excellent flexibility in sensor design. In this study, we use a Wavelength-Division Multiplexing (WDM)-based fiber system. Although other multiplexing methods (e.g., Optical Frequency Domain Reflectometry, or OFDR) can provide a greater number of FBGs per fiber, WDM offers low cost, simplicity, and high frequency sampling [20].

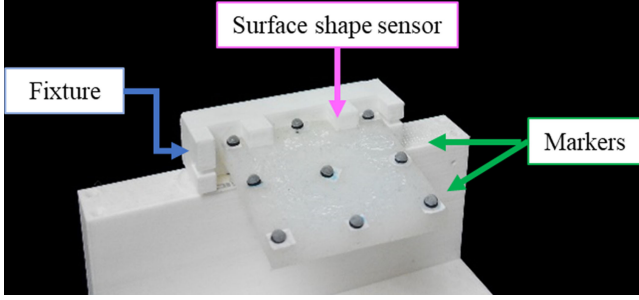


Fig. 5. Experimental setup for training data collection. The sensor is covered with 9 IR-tracking markers and clamped on a fixture. Their 3D positions tracked by two Optitrack Flex 3 cameras are collected as data outputs of the ANN.

### III. EXPERIMENTAL SETUP AND RESULTS

#### A. Data Input and Sampling for Model Training

The unique strain-shape mapping for surface shape reconstruction has been investigated with FEA. The corresponding surface sensor is also fabricated. Experiments are designed to validate the sensing performance and characteristics. Such validation requires ground truth data that represents the surface morphology. In our setup as shown in Fig. 5, our fabricated sensor is clamped at one side to ease the validation. *Nine* grid points on the sensor surface were chosen, where reflective markers were attached. Their 3D positions were measured by two infrared (IR) tracking cameras (Optitrack Flex 3). The tracking rate was 100 fps and the mean positional error was 0.015 mm.

An invisible broadband light (Amonics ALS-CL-18) is transmitted to the optical fiber via an optical circulator (PIOC-3-CL). Light is reflected due to the change in core refractive index which is strain dependent. The reflected spectrum is sent to a small FBG interrogator (I-MON 512 USB) from the output port of the optical circulator. This interrogator can detect and identify over 70 FBGs with a wavelength resolution  $>0.5$  pm and a maximum measuring frequency of 3000 Hz.

To build a learning model for the real sensing, 1000 IR-tracked sensor configurations, along with their corresponding Bragg spectrum, are captured, then used for ANN training with L-M backpropagation. Since there would be fabrication defects, such as fiber dislocations within the silicone substrate or uneven stiffness distribution, it is advantageous that no calibration is required. Any error caused by these defects are compensated by the ANN training. Those defects exist even with industrial manufacturing processes and are difficult to be considered in analytical models.

#### B. Surface Reconstruction Performance

The sensor was bent and twisted manually to form various, complex configurations, but also without blocking any of the 9 optical markers from the IR-tracking. At each time point, 16 Bragg wavelengths were measured. The shifted wavelengths act as *inputs*, which are proportional to the actual change of strain at the corresponding FBG location. Displacements of the 9 markers in 3D, *twenty-seven* ( $9 \times 3$ ) variables in total, are then defined as *outputs*. The ANN will, thereby, model such a mapping from these inputs to outputs (Training time: 4s, Window10, 8G RAM,

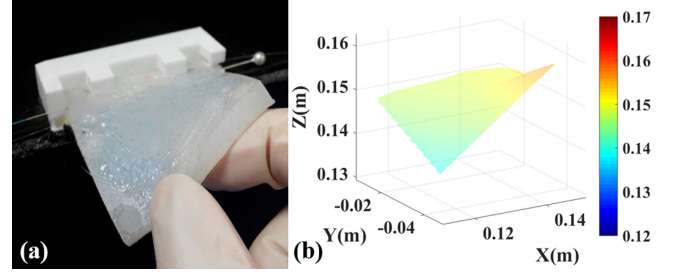


Fig. 6. A surface shape reconstruction example. (a) A force is applied to the sensor and causes deformation of the sensor surface, and (b) The sensor surface is reconstructed by the trained neural network. The colormap indicates the depth of the surface.

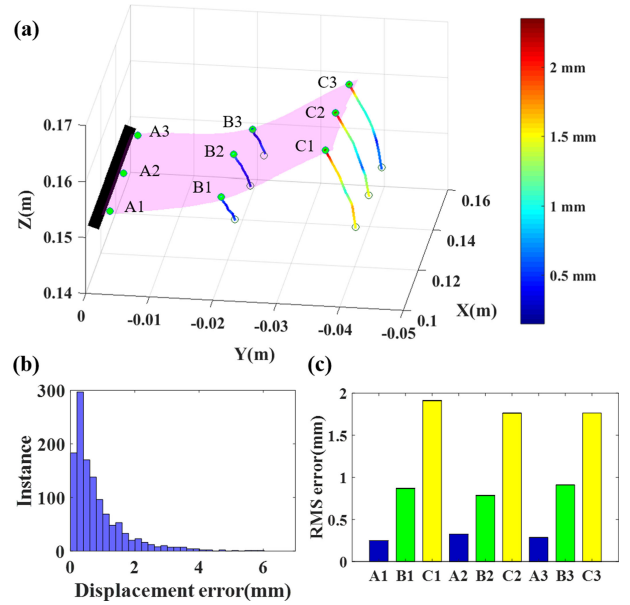


Fig. 7. Accuracy analysis of the surface shape reconstruction: (a) A surface reconstruction sample with colored trajectories of nine nodes, where the color indicates the corresponding displacement errors during bending. (b) Displacement error distribution of all nodes. (c) Root-mean-square error (RMSe) of all node displacements.

i7-7500U). A linearly-interpolated surface is fitted by the output nodes. Fig. 6 shows an example of our shape sensing, where the surface is reconstructed based on displacement coordinates estimated by the ANN outputs. Real-time sensing performance is also demonstrated in the attached video, in which the soft sensor was deformed (bended/twisted) manually. The reconstructed surface motion was obtained in sync with the deformation. The surface reconstruction update frequency is approximately 10 Hz within the Matlab environment.

The sensing error can be obtained by comparing the ANN-estimated output coordinates with the IR-tracking ground truth. A sample deformation case is shown in Fig. 7(a), where the sensor was bent up from the neutral position. Colored trajectories of the nine markers were recorded. The warmer the color the bigger the displacement errors, relative to the ground truth. Fig. 7(b) shows the histogram of such errors throughout 1350 instance samples. The majority of node displacement errors were below 2 mm. Larger errors are seen in nodes further from the clamped side (fixed end), i.e.,  $C1 \sim C3$  in Fig. 7(a). The



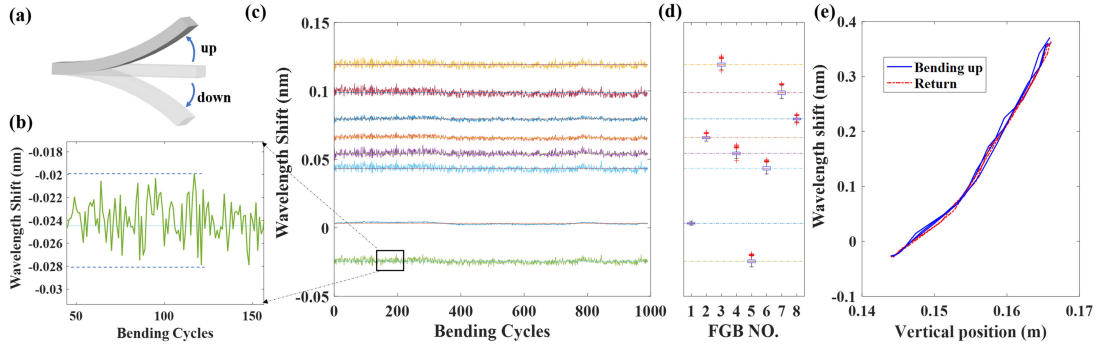


Fig. 8. Repeatability tests of the proposed shape sensor under periodic loading. (a) Sensor is clamped to a fixture, and bent along the free end by 3 linear actuators. 1000 cycles of such bending were conducted in 50 min. (b) Zoomed in view of wavelength shift fluctuation. (c) Wavelength shifts of the 8 FBGs on the first layer were recorded at the peak of upward bending. Over the cycles, the shift values showed small fluctuations about a constant. (d) Boxplot showing the distributions of wavelength shift. Fluctuation for all FBGs was less than 0.01 nm, corresponding to 0.3 mm displacement. (e) Hysteresis plot comparing vertical position of the distal node C2 and wavelength shift of the FBG with largest shift. The sensor was bent up and returned to the flat position for 3 cycles.

root-mean-square error (RMSe) was about 1.8 mm for nodes  $C1 \sim C3$ . In contrast, the nodes  $A1 \sim A3$ , and  $B1 \sim B3$  had smaller errors, with RMSe at 1.17 mm across all nodes. In general, the node displacement errors increased with the distance from the fixed end. This could be attributed to the distribution of node positions in the ANN training data. Every node has the same total samples, however the nodes at the free end,  $C1 \sim C3$ , have a larger displacement range, when compared with nodes  $A1 \sim A3$  and  $B1 \sim B3$ . This results in less spatially dense sample points, and hence poorer training performance for the distal nodes. This may be a primary cause for the increased reconstruction error at nodes  $C1 \sim C3$  (Fig. 7(c)).

Reliability tests were performed to ensure consistent responses over a long operating period. Numerous repeated cycles of sensor motion were generated by 3 linear actuators, which pushed/pulled the nodes  $C1 \sim C3$ . As illustrated in Fig. 8(a), the sensor was bent upward, downward and finally back to the neutral position in 2 seconds. A total of 1000 bending cycles were conducted over 50 min, with Bragg wavelength responses recorded at the peak of upward motion. Fig. 8(c) shows the reflected wavelength shift of eight FBGs on a layer. It can be observed that the wavelength shift values fluctuate slightly around a constant value. The boxplot (Fig. 8(d)) shows distributions of the eight wavelength shifts. The wavelength fluctuations remained below 0.01 nm for all FBGs, corresponding to 0.3 mm displacement. This indicates that the sensor can maintain stable and reliable responses throughout 1000 deformation cycles.

The signal-to-noise ratio (SNR) for the bent-up configuration is 14.9 dB, calculated by comparing the vertical displacements of the distal node and noise. The hysteresis of the sensor was also evaluated by repeatedly displacing the distal side of the sensor (nodes  $C1$  to  $C3$ ) upwards by 20 mm and returning to the neutral flat position (3 cycles at  $\sim 1$  Hz). The vertical displacement was provided by a linear actuator, and the vertical position of the node  $C2$  and the wavelength shift of the FBG with largest shift was recorded. Small disparity between the bending up and return motion was found, as illustrated in Fig. 8(e), suggesting a low level of hysteresis in the presented sensor. To test the resolution of the sensor, a range of vertical displacement steps ranging from 0.1 mm to 1 mm were applied to the distal sensor side. The sensor could detect displacement changes down to the applied

0.1 mm displacement, suggesting that the sensor resolution is 0.1 mm or lower.

Despite the reasonable flexibility and stretchability of our sensor prototype, the allowable strain caused by purely in-plane loading is still small. It is limited by the rigid optical fiber that constrains the deformation. In combination with the sensor's small size, more complex deformations could not be measured without risk of damage to the fiber. The sensor flexibility could be further enhanced by altering the fiber layout, but this requires consideration of other factors such as fiber length, number of FBGs, as well as the trade-off against the overall sensor sensitivity. Another limitation of the proposed sensor is the pressure sensitivity. Applying pressure to the sensor can induce strain in the FBGs without causing large deformation of the surface itself. This may cause incorrect shape reconstruction using our current approach. We will investigate techniques capable of distinguishing local pressure stimuli from the general shape reconstruction. This could enable simultaneous measurement of shape and force, which is particularly important for haptics applications, and ultimately reduce reconstruction error. Furthermore, in this letter we compensate ambient temperature changes near the sensor, however there is still difficulty in compensating local temperature changes for each FBG, which is an inherent disadvantage of using one single-core fiber.

#### IV. CONCLUSION

In this letter, a high-performance surface shape sensor is presented. Provided with sparsely distributed strain measured by FBGs along a single-core optical fiber, we have demonstrated that the soft sensor surface shape can be promptly reconstructed using a machine learning algorithm. The sensor makes use of sparse FBG data provided by a WDM-based fiber system. Prior to our real sensor fabrication, we have also conducted FEA to characterize the sensor parameters, such as to predict the sensing strains and their accuracy, as well as the uniqueness of mapping between the fiber strains and the sensor surface. Our proposed sensor prototype has been tested to virtually reconstruct a flexible surface in real-time. The sensing accuracy and reliability have also been experimentally validated. The sensor achieved an accuracy of RMSe =

1.17 mm for reconstructed node displacements, which is also a reflection of the dependence on training data quality. For 1000 repeated cycles of motion applied on the sensor, the measured node displacements remained under 0.3 mm, demonstrating reliability in response to the repeated deformation. In general, these outperform various electronics-based shape sensors, (despite just very few reported) particularly in the aspects of complicated fabrication, electrodes and cables handling.

Based on the proposed design framework, a sensor could be used on the surface of a soft robot to improve interaction with the environment. This could aid in advanced soft robotic control where haptic sensing and locating contact on the soft robot body is a difficult task with current sensors. A similar application of the sensor is for enhancing rigid-link robots. The sensor could be integrated as both a soft, pliable layer, and a surface/contact sensor for enabling close interaction with the environment. For applications as a wearable device (e.g., rehabilitation), the sensor would closely interact with the body. For complex deformations like in a shoulder joint, the original sensor shape should be customized to the anatomy, which may increase the difficulty in fabrication. Although with our framework, complex, task-specific modeling is not required, care must be taken to minimize the sensor's effect on the wearer (human or robot) and not change their intrinsic deformability.

Regarding cost, fiber-based shape sensors commonly make use of multiple-core fiber paired with OFDR-based measurement systems, which are substantially more expensive (>USD160K) and complex to implement, relative to our WDM-based, single-core fiber system (<USD20K).

A number of limitations still exist for the proposed sensor. Firstly, by making use of a learning-based modeling approach, inherent disadvantages arise relating to data acquisition time and reliance on accurate training data. Additionally, the proposed sensor design has a limited ability to reconstruct very complex shapes, due to the inherent rigidity of optical fiber in combination with the small sensor size. In future studies, we will propose an FEA-based optimization scheme to investigate ideal optical fiber layouts for complex deformations or customized shape structures (e.g., tube reconstruction in the supplementary video). We also aim to accelerate the reconstruction speed by exploring other plotting environments and implementation on higher performance hardware.

## REFERENCES

- [1] K.-H. Lee *et al.*, "Nonparametric online learning control for soft continuum robot: An enabling technique for effective endoscopic navigation," *Soft Robot.*, vol. 4, no. 4, pp. 324–337, 2017.
- [2] P. Polygerinos, Z. Wang, K. C. Galloway, R. J. Wood, and C. J. Walsh, "Soft robotic glove for combined assistance and at-home rehabilitation," *Robot. Auton. Syst.*, vol. 73, pp. 135–143, 2015.
- [3] C. Laschi, B. Mazzolai, and M. Cianchetti, "Soft robotics: Technologies and systems pushing the boundaries of robot abilities," *Sci. Robot.*, vol. 1, no. 1, 2016, Art. no. eaah3690.
- [4] G. Sansoni *et al.*, "State-of-the-art and applications of 3D imaging sensors in industry, cultural heritage, medicine, and criminal investigation," *Sensors*, vol. 9, no. 1, pp. 568–601, 2009.
- [5] F. Saunders, E. Golden, R. D. White, and J. Rife, "Experimental verification of soft-robot gaits evolved using a lumped dynamic model," *Robotica*, vol. 29, no. 6, pp. 823–830, 2011.
- [6] M. K. Dobrzynski *et al.*, "Contactless deflection sensor for soft robots," in *Proc. IEEE/RSJ Int. Conf. Intell. Robots Syst.*, 2011, pp. 1913–1918.
- [7] W. Yuan, S. Dong, and E. H. Adelson, "GelSight: High-resolution robot tactile sensors for estimating geometry and force," *Sensors*, vol. 17, no. 12, Nov. 29, 2017, Art. no. E2762.
- [8] K. Sato, K. Kamiyama, N. Kawakami, and S. Tachi, "Finger-shaped gel force: Sensor for measuring surface traction fields for robotic hand," *IEEE Trans Haptics*, vol. 3, no. 1, pp. 37–47, Jan.–Mar. 2010.
- [9] A. Hermanis, R. Cacurs, and M. Greitans, "Acceleration and magnetic sensor network for shape sensing," *IEEE Sensors J.*, vol. 16, no. 5, pp. 1271–1280, Mar. 2016.
- [10] A. Hermanis and K. Nesenbergs, "Grid shaped accelerometer network for surface shape recognition," in *Proc. 13th Biennial Baltic Electron. Conf.*, 2012, pp. 203–206.
- [11] P. Mittendorf and G. Cheng, "3D surface reconstruction for robotic body parts with artificial skins," in *Proc. IEEE/RSJ Int. Conf. Intell. Robots Syst.*, 2012, pp. 4505–4510.
- [12] N. Saguin-Sprynski, L. Jouanet, B. Lacolle, and L. Biard, "Surfaces reconstruction via inertial sensors for monitoring," in *Proc. 7th Eur. Workshop Struct. Health Monitoring*, 2014, pp. 702–709.
- [13] Y.-L. Park, B.-R. Chen, and R. J. Wood, "Design and fabrication of soft artificial skin using embedded microchannels and liquid conductors," *IEEE Sensors J.*, vol. 12, no. 8, pp. 2711–2718, Aug. 2012.
- [14] V. Wall, G. Zöller, and O. Brock, "A method for sensorizing soft actuators and its application to the RBO hand 2," in *Proc. IEEE Int. Conf. Robot. Automat.*, 2017, pp. 4965–4970.
- [15] H.-N. Li, D.-S. Li, and G.-B. Song, "Recent applications of fiber optic sensors to health monitoring in civil engineering," *Eng. Struct.*, vol. 26, no. 11, pp. 1647–1657, 2004.
- [16] G. C. Kahandawa, J. Epaarachchi, H. Wang, and K. Lau, "Use of FBG sensors for SHM in aerospace structures," *Photon. Sensors*, vol. 2, no. 3, pp. 203–214, 2012.
- [17] K. O. Hill and G. Meltz, "Fiber Bragg grating technology fundamentals and overview," *J. Lightw. Technol.*, vol. 15, no. 8, pp. 1263–1276, Aug. 1997.
- [18] P. Wei, J. Liu, Z. Dai, and M. Li, "Monitoring the shape of satellite wing frame using FBG sensors in high electronic noise, vacuum, and—196 °C ENVironment," *IEEE Trans. Ind. Electron.*, vol. 64, no. 1, pp. 691–700, Jan. 2017.
- [19] B. A. Childers *et al.*, "Use of 3000 Bragg grating strain sensors distributed on four 8-m optical fibers during static load tests of a composite structure," in *Proc. Smart Struct. Mater. Ind. Commercial Appl. Smart Struct. Technol.*, vol. 4332, pp. 133–143, 2001.
- [20] M. Amanzadeh *et al.*, "Recent developments in fibre optic shape sensing," *Measurement*, vol. 128, pp. 119–137, 2018.
- [21] S. C. Ryu and P. E. Dupont, "FBG-based shape sensing tubes for continuum robots," in *Proc. IEEE Int. Conf. Robot. Automat.*, 2014, pp. 3531–3537.
- [22] C. Shi *et al.*, "Shape sensing techniques for continuum robots in minimally invasive surgery: A survey," *IEEE Trans. Biomed. Eng.*, vol. 64, no. 8, pp. 1665–1678, Aug. 2017.
- [23] A. F. da Silva, A. F. Gonçalves, P. M. Mendes, and J. H. Correia, "FBG sensing glove for monitoring hand posture," *IEEE Sensors J.*, vol. 11, no. 10, pp. 2442–2448, Oct. 2011.
- [24] L. Xu, J. Ge, J. H. Patel, and M. P. Fok, "3-Dimensional soft shape sensor based on dual-layer orthogonal fiber Bragg grating mesh," in *Proc. Opt. Fiber Commun. Conf. Exhib.*, 2017, pp. 1–3.
- [25] H. Zhang, X. Zhu, Z. Gao, K. Liu, and F. Jiang, "Fiber Bragg grating plate structure shape reconstruction algorithm based on orthogonal curve net," *J. Intell. Mater. Syst. Struct.*, vol. 27, no. 17, pp. 2416–2425, 2016.
- [26] S. Rapp, L.-H. Kang, U. C. Mueller, J.-H. Han, and H. Baier, "Dynamic shape estimation by modal approach using fiber Bragg grating strain sensors," in *Proc. Sensors Smart Struct. Technol. Civil, Mech., Aerosp. Syst.*, 2007, vol. 6529, Art. no. 65293.
- [27] R. Kashyap, *Fiber Bragg Gratings*. New York, NY, USA: Academic, 2009.
- [28] M. Kreuzer, "Strain measurement with fiber Bragg grating sensors," HBM, Darmstadt, Germany, White Paper, S2338-1.0 e, 2006.
- [29] P. Moseley, J. M. Florez, H. A. Sonar, G. Agarwal, W. Curtin, and J. Paik, "Modeling, design, and development of soft pneumatic actuators with finite element method," *Adv. Eng. Mater.*, vol. 18, no. 6, pp. 978–988, 2016.
- [30] D. Coric, M. Lai, J. Botsis, A. Luo, and H. G. Limberger, "Distributed strain measurements using fiber Bragg gratings in small-diameter optical fiber and low-coherence reflectometry," *Opt. Express*, vol. 18, no. 25, pp. 26484–26491, 2010.